Interaction Large-Signal Stability Analysis of M3C and GFM/GFL Hybrid Control Strategies Converters Based on the Novel Fuzzy Tensor Space Method

Ziyue Duan, *Student Member, IEEE*, Yongqing Meng, *Member, IEEE*, Peiqi Zhao, *Student Member, IEEE*, Shuhao Yan, *Student Member, IEEE*, Xiuli Wang, *Senior Member, IEEE*, and Xifan Wang, *Fellow, IEEE*

***Abstract*—This article proposes a novel fuzzy tensor space method to analyze the interaction large-signal stability of modular multilevel matrix converter and grid-forming/following (GFM/GFL) hybrid control strategy converters. By addressing the challenges of high-order, strong nonlinearity, and multi-frequency coupling in the system's dynamic model, the complexity is reduced from exponential to constant levels using sector nonlinearity theory. It is achieved by optimizing the original membership function set into a linearly independent fuzzy tensor basis. In addition, leveraging the physical significance of the fuzzy tensor space reduces the mapping area for solving the Lyapunov functional problem, effectively lowering the conservatism. Furthermore, the stability analysis results obtained from this method offer a better balance of complexity and accuracy compared to traditional TS fuzzy theory. Based on the improved method, the complex coupling stability mechanism caused by the interaction of multiple power electronic devices and control strategies can be analyzed quickly and accurately. In particular, these results are used to study the impact of different configurations of GFM/GFL converters under various disturbance conditions, as well as the interaction stability mechanism of different configuration ratios combined with grid strength. Finally, the validity of these results is confirmed through theoretical and experimental verification.**

***Index Terms*—Fuzzy tensor space method, grid-forming/following (GFM/GFL), large-signal stability, modular multilevel matrix converter (M3C).**

NOMENCLATURE

ω_{FL}/ω_{FM}	Angular frequency of GFL/GFM.
ω_{MI}	Angular frequency of MI side.
ω_{ML}	Angular frequency of ML side.
$\overline{V}_{dc}^{M}$	M3C DC voltage.
$\mathbf{x}_{dq}$	$\mathbf{x}$ in corresponding dq coordinate system.
$\mathbf{x}_{ref}/\mathbf{x}^{0}$	Reference value of $\mathbf{x}$.
C_{ML}	M3C ML filter capacitor.
E_{uvw}	Industrial frequency power voltage.
i^{FL}/i^{FM}	GFL/GFM converters output current.
i_{abc}^{ML}	M3C ML side current.
i_{gabc}^{ML}	Common bus current.
$J/D/\Lambda$	Inertia and damping of GFM converter.
k_{pi}^{FL}	PI parameters of GFL converter outer loop.
k_{pi}^{FLP}	PI parameters of GFL converter PLL.
k_{pi}^{FM}	PI parameters of GFM converter outer loop.
k_{pi}^{MIP}	PI parameters of M3C MI PLL.
k_{pi}^{MI}	PI parameters of M3C MI outer loop.
k_{pi}^{ML}	PI parameters of M3C ML outer loop.
L_{FL}/C_{FL}	GFL converter filter parameters.
L_{FM}/C_{FM}	GFM converter filter parameters.
L_M	M3C arm-bridge inductor.
P^{FL}/P^{FM}	GFL/GFM converters active power.
Q^{FL}/Q^{FM}	GFL/GFM converters reactive power.
Q_{MI}	M3C MI side reactive power.
R_g^{FL}/L_g^{FL}	GFL converter line parameters.
R_g^{FM}/L_g^{FM}	GFM converter line parameters.
R_L/L_L	Common bus parameters.
u_{abc}^{ML}	M3C ML side voltage.
u_c^{FL}/u_c^{FM}	GFL/GFM converters output voltage.
u_{uvw}^{MI}	M3C MI side voltage.

Received 27 September 2024; revised 21 January 2025; accepted 25 February 2025. Date of publication 28 February 2025; date of current version 14 April 2025. This work was supported by the National Natural Science Foundation of China under Grant 52477121 "Research on Key Technologies for Flexible Power Regulation and Operation Control in Multi-frequency Power Systems with Large-scale Renewable Energy Integration". Recommended for publication by Associate Editor F. W. Fuchs. *(Corresponding author: Yongqing Meng.)*

The authors are with the School of Electrical Engineering, Xi'an Jiaotong University, Xi'an 710049, China (e-mail: mengyq@mail.xjtu.edu.cn).

Color versions of one or more figures in this article are available at https://doi.org/10.1109/TPEL.2025.3546736.

Digital Object Identifier 10.1109/TPEL.2025.3546736

I. INTRODUCTION

MODULAR multilevel technology has become the most promising option for the design of converter topology in medium and high voltage industrial applications. As the global low-carbon process accelerates, a direct ac/ac converter known as modular multilevel matrix converter (M3C), which boasts excellent scalability and high reliability, has found wide applications in renewable energy power conversion, all-electric marine vessel propulsion, railway electric traction, and industrial motor drives [1], [2].

The typical M3C topology, illustrated in Fig. 1, comprises nine bridge arms, each containing a series-connected full-bridge submodule and an inductor, enhancing the system's redundancy and reliability. And without requiring a dc link, M3C directly converts ac power on both sides. Consequently, in high-power energy conversion and variable-speed drive applications, M3C is often connected to industrial motors or power grids on one

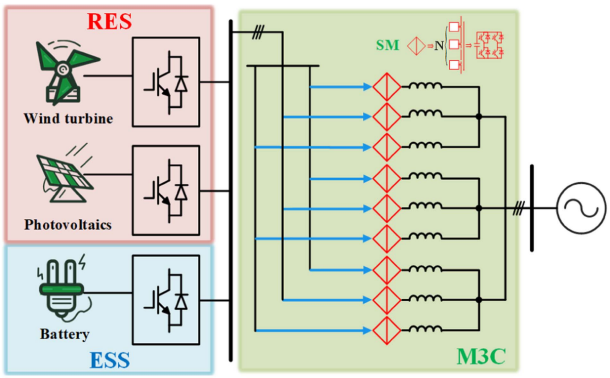

Fig. 1. Interaction system of M3C with GFM/GFL hybrid control strategies converters.

side and to renewable energy sources such as wind power, photovoltaics, and energy storage via grid-connected converters on the other side [3], [4]. These renewable energy grid-connected converters typically employ control strategies tailored to the energy source, including grid-forming (GFM) and grid-following (GFL) types [5]. Due to the issues associated with using either the GFM or GFL control strategy individually, such as GFL's tendency to cause stability problems under weak grid conditions, and GFM's loss of dynamic tracking speed due to the lack of an inner loop hybrid approach, combining both control strategies, is currently widely employed [6]. It involves the integration of multiple power electronic converters with different control strategies, which, by complementing the advantages of each, ensures the stable operation of the overall system [7]. Furthermore, when large-signal disturbances, such as power fluctuations or line faults, the interaction between grid-connected converters with different control strategies and the M3C can trigger various unstable modes, jeopardizing the safe and stable operation [8], [9], [10]. However, due to the complexity of control strategies, high-order dynamic models, and multifrequency coupling in such GFM/GFL hybrid control strategies converter and M3C interaction system, analyzing their large-signal stability interactions has become a focal point in M3C industrial applications.

Many scholars have investigated these issues, but some gaps remain. Stability research on complex interconnected power electronic systems has predominantly focused on small-signal analysis, with methods such as impedance analysis, state-space model, and harmonic state-space theory [11], [12]. However, when power electronic devices face large-signal disturbances, the steady-state operating point shifts after the transient process [13], making small-signal linearization inadequate.

Therefore, the interaction large-signal stability must be thoroughly analyzed using Lyapunov stability criteria, which involve energy functions and attraction domain. Consequently, scholars have proposed various methods for constructing Lyapunov functions in multiconverter interaction systems within power transmission field and microgrids, including the direct method [14], [15], mixed potential function [16], [17], artificial intelligence method [18], [19], and sector nonlinearity theory [20], [21], [22], [23]. However, on one hand, due to the high order and strong nonlinearity, it is challenging to directly provide a well-established Lyapunov function similar to that for synchronous machine. In addition, methods such as TS fuzzy models, and sum-of-squares (SOS) optimization based on sector nonlinearity theory face dimensionality issues due to the excessive number of nonlinear terms. On the other hand, simplifying the system by ignoring some nonlinear dynamics can compromise the conservatism of the attraction domain results, leading to inaccurate stability analysis. In conclusion, for analyzing the large-signal stability interactions in the complex interconnected system of M3C and GFM/GFL hybrid converters, a method that balances computational efficiency and accuracy is still required.

In addition, artificial intelligence methods simulate the Lyapunov function using neural networks. While their strong nonlinear fitting capabilities can address some functional problems, these black-box approaches cannot analyze the mechanisms of instability in the solutions. For example, the impact of the proportional configuration of GFM and GFL converters on stability and the transmission of disturbances across different locations and types among multiple power electronic devices present new analytical challenges [24], [25], [26].

To address these issues, this article makes the following contributions: Firstly, it establishes a dynamic model of the interaction system of M3C and GFM/GFL hybrid control strategy converters, considering their multifrequency coupling characteristics and retaining their high-order and strong nonlinear features. Then, based on sector nonlinearity theory, the complexity of constructing the fuzzy model system is reduced from exponential to constant by optimizing the linear independent combinations in the original membership functions and extracting the fuzzy tensor basis. Furthermore, by integrating the physical significance of the fuzzy tensor space, the mapping area is optimized, reducing the conservatism of the attraction domain obtained from solving the linear matrix inequality (LMI) problem. By comparing the novel fuzzy tensor space method with traditional TS fuzzy theory and higher-order SOS methods, it is shown to balance complexity and accuracy effectively. Finally, based on the stability analysis results, the study examines how different configurations of GFM and GFL converters impact system stability under various disturbance conditions. And the impact mechanism of different configuration ratios and grid strength on system interaction stability is analyzed by incorporating the interfrequency interaction characteristics. In conclusion, this article provides a reference framework for the novel analysis of large-signal stability in complex multimachine and multifrequency interacting power electronic converter systems. Building on the improved method, the complex stability mechanisms arising from the interactions between multiple power electronic devices and the coupling of various control strategies can be efficiently and accurately analyzed.

The rest of this article is organized as follows. Section II covers the dynamic modeling of the interaction system. Section III presents the novel fuzzy tensor space method. Section IV validates the results through theoretical and experimental verification. Finally, Section V concludes this article.

II. System Modeling and Problem Formulation

The system for analyzing the large-signal interaction stability between M3C and grid-connected converters with different

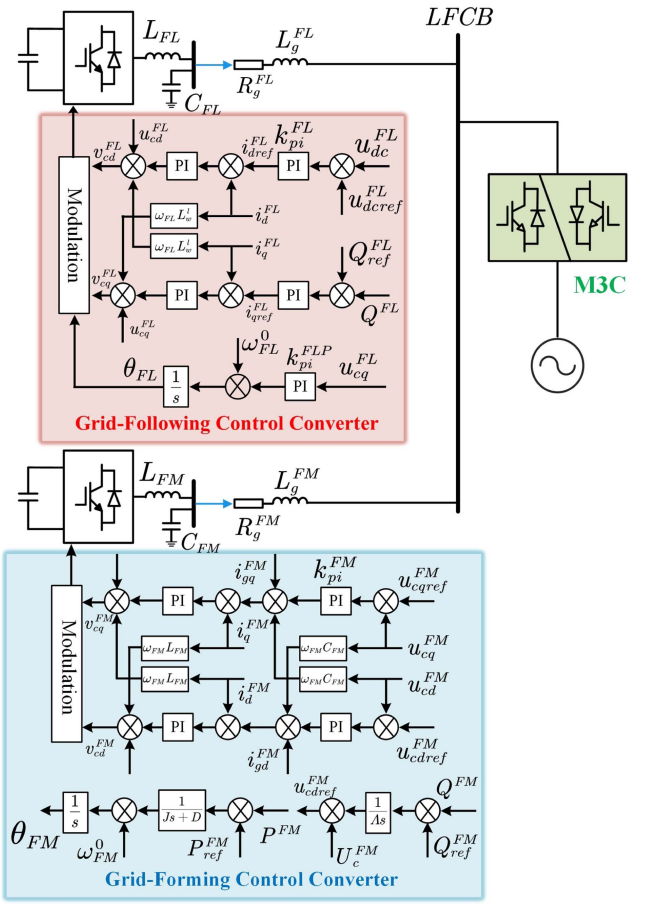

Fig. 2. GFM/GFL control strategies for the hybrid grid-connected converters.

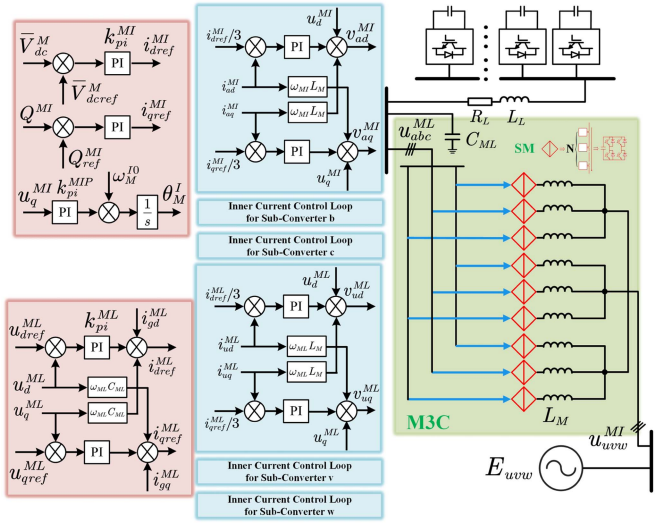

Fig. 3. Control strategies for the M3C.

control modes is shown in Fig. 1. It is worth noting that to investigate the large-signal stability mechanism of grid-connected converters using GFM/GFL hybrid control strategies in low-frequency systems, we simplify the structure, without loss of generality, to a configuration in which two converters with different control strategies are connected in parallel to the same low-frequency bus. By neglecting the internal coupling within converters using the same control strategy, we focus primarily on the interaction mechanisms between converters with different control strategies and between these converters and the M3C. Thus it can be divided into three parts: 1) the GFL/GFM converters; 2) the connecting lines; and 3) the M3C.

As for part I, to simplify the analysis, these converters are further integrated into two parallel VSCs, each employing either GFL or GFM control strategies, as illustrated in Fig. 2. First, the outer loop of the GFL control strategy regulates the dc capacitor voltage v_{dc}^{FL} and reactive power Q^{FL}, of which dynamic model can be represented as

$$\begin{cases} i_{dref}^{FL} = k_p^{FL}\Delta v_{dc}^{FL} + k_i^{FL} s_{dc}^{FL} & \dot{s}_{dc}^{FL} = \Delta v_{dc}^{FL} \\ i_{qref}^{FL} = k_p^{FL}\Delta Q^{FL} + k_i^{FL} s_Q^{FL} & \dot{s}_Q^{FL} = \Delta Q^{FL} \end{cases} \tag{1}$$

where Δ represents the difference between the relevant variables and their corresponding steady-state values and i_{dq}^{FL} represents the output current of the GFL converter in the dq reference frame. Furthermore, considering that the dynamic response of the inner loop is significantly faster than that of the outer loop, the inner loop dynamics can be neglected [13]. Then, the PLL calculates the phase using the voltage at PCC and its dynamic expression is given by

$$\omega_{FL} = k_p^{FLP} u_{cq}^{FL} + k_i^{FLP} s_P^{FL} + \omega_{FL}^0 \quad \dot{s}_P^{FL} = u_{cq}^{FL}. \tag{2}$$

Finally, the dynamic expression of the GFL filter circuit can be written as

$$\begin{cases} L_{FL}\dot{i}_{dq}^{FL} = u_{dq}^{FL} - u_{cdq}^{FL} \pm \omega_{FL} L_{FL} i_{qd}^{FL} \\ C_{FL}\dot{u}_{cdq}^{FL} = i_{dq}^{FL} - i_{gdq}^{FL} \pm \omega_{FL} C_{FL} u_{cqd}^{FL}. \end{cases} \tag{3}$$

In contrast, the GFM control strategy simulates the dynamic characteristics of a virtual synchronous machine to provide inertia support. Its dynamic model can be represented as

$$J\dot{\omega}_{FM} = \Delta P^{PM} - D\omega_{FM} \quad \Lambda \dot{u}_{cdref}^{FM} = \Delta Q^{FM} \tag{4}$$

where J and D represent the inertia constant and damping coefficient of GFM converter. Furthermore, the dynamic expression of the GFM filter circuit can be represented as

$$\begin{cases} L_{FM}\dot{i}_{dq}^{FM} = u_{dq}^{FM} - u_{cdq}^{FM} \pm \omega_{FM} L_{FM} i_{qd}^{FM} \\ C_{FM}\dot{u}_{cdq}^{FM} = i_{dq}^{FM} - i_{gdq}^{FM} \pm \omega_{FM} C_{FM} u_{cqd}^{FM}. \end{cases} \tag{5}$$

In allusion to part II, the GFL and GFM converters connect to the grid or supply power to loads via the low-frequency common bus (LFCB) after being processed by the M3C. Regarding the selection of LFCB frequency, [27] provides large-signal stability analysis for offshore wind power low-frequency systems. However, in the analysis of the interaction between VSC and M3C hybrid power electronic devices, without considering economic conditions, the analysis can initially be based on one-third of the industrial frequency, according to the static stability limit formula. If the voltage of the LFCB is defined as u_{cdq}^{LF}, then the dynamic expression between the GFL/GFM converter and the

bus can be expressed as

$$\begin{cases} u_{cdq}^{FL} - u_{cdq}^{LF} = R_g^{FL} i_{gdq}^{FL} + L_g^{FL} \dot{i}_{gdq}^{FL} \mp \omega_{FL}^0 L_g^{FL} i_{gqd}^{FL} \\ u_{cdq}^{FM} - u_{cdq}^{LF} = R_g^{FM} i_{gdq}^{FM} + L_g^{FM} \dot{i}_{gdq}^{FM} \mp \omega_{FM}^0 L_g^{FM} i_{gqd}^{FM} \end{cases} \tag{6}$$

On the other hand, calculating from the bus to the low-frequency side of the M3C, the relationship between the bus node current and the bus voltage can be derived as $i_{gdq}^{FL} + i_{gdq}^{FM} + i_{gdq}^{ML} = 0$. Then, the dynamics expression corresponding to the voltage of the M3C and LFCB can also be expressed by

$$\begin{cases} u_{cd}^{LF} - u_d^{ML} = R_L i_{gd}^{ML} + L_L \dot{i}_{gd}^{ML} - \omega_{ML}^0 L_L i_{gq}^{ML} \\ u_{cq}^{LF} - u_q^{ML} = R_L i_{gq}^{ML} + L_L \dot{i}_{gq}^{ML} + \omega_{ML}^0 L_L i_{gd}^{ML}. \end{cases} \tag{7}$$

Finally, in Part III, the low-frequency (ML) and high-frequency (MI) sides of the M3C are controlled using distinct strategies: the GFM control for the ML side and the GFL control for the MI side. The M3C is composed of nine bridge arms that serve as the critical components connecting the two frequency domains in the circuit structure, facilitating direct ac/ac frequency conversion [28]. Each of the nine arms is designed to incorporate two frequency components, which are coupled together. The energy transfer between these components occurs through the capacitors located in the submodules. To ensure efficient frequency decoupling control within the M3C, it is essential that the electrical components within each arm undergo Park transformations at both the low and high frequencies. This transformation allows the decomposition of the system into distinct components, enabling independent control and synthesis of the MI and ML frequency components [29], [30], [31]. This control strategy ensures that the different frequency domains of the M3C can operate independently, which enhances its overall performance and stability.

On the ML side, M3C uses the Vf-based GFM control strategy to provide frequency support for the VSC grid connection. Since the VSC part employs a hybrid GFL and GFM grid connection control strategy, the ML side is required to provide voltage and angular frequency phase references with sufficient active support capability. Compared to the VSC with the GFM control strategy, the M3C has a larger capacity and greater inertia. In power electronic interconnected systems with low-frequency integration of renewable energy, the introdution of the Vf-based GFM control strategy on the ML side is more reasonable. Thus, the dynamic model of its outer loop is related to the voltage of the parallel capacitor at the ML port and can be specifically represented as

$$\begin{cases} i_d^{ML} = i_{gd}^{ML} + k_p^{ML} \Delta u_d^{ML} + k_i^{ML} s_{ud}^{ML} - \omega_{ML}^0 C_g^{ML} u_q^{ML} \\ i_q^{ML} = i_{gq}^{ML} + k_p^{ML} \Delta u_q^{ML} + k_i^{ml} s_{uq}^{ML} + \omega_{ML}^0 C_g^{ML} u_d^{ML} \end{cases} \tag{8}$$

where i_{dq}^{ML} represent the output current of M3C ML side, and i_{gdq}^{ML} represent the current in the connection line between M3C and the grid-connected converters. It should be noted that the voltage regulation and circulating current control strategies of M3C belong to the modulation part, which follows a similar principle to the simplification of the inner loop dynamics. In the context of large-signal disturbances and the analysis of the mixed interaction and coupling stability mechanisms of multiple power electronic devices focused on in this article, corresponding simplifications can be applied.

On the other hand, on the MI side, the M3C utilizes a GFL control strategy to connect with an industrial frequency source or industrial motor, enabling industrial operations such as stirring and heating for load management or motor driving applications. Therefore, the dynamic expression of the outer loop is given by

$$\begin{cases} i_{dref}^{MI} = k_p^{MI} \Delta \bar{V}_{dc}^{MI} + k_i^{MI} s_{dc}^{MI} \ \dot{s}_{dc}^{MI} = \Delta \bar{V}_{dc}^{MI} \\ i_{qref}^{MI} = k_p^{MI} \Delta Q^{MI} + k_i^{MI} s_Q^{MI} \ \dot{s}_Q^{MI} = \Delta Q^{MI}. \end{cases} \tag{9}$$

Furthermore, assuming the industrial frequency source voltage is constant and connected to the MI side of M3C through one transmission line, combined with the PLL dynamics on the MI side, its model can be represented as

$$\begin{cases} \omega_{MI} = k_p^{MIP} u_q^{MI} + k_i^{MIP} s_P^{MI} + \omega_{MI}^0 \quad \dot{s}_P^{MI} = u_q^{MI} \\ u_q^{MI} = E_g \sin\theta_{MI} - \left(R_g i_q^{MI} + L_g \dot{i}_q^{MI} + \omega_{MI}^0 L_g i_d^{MI} \right). \end{cases} \tag{10}$$

In summary, all state variables of the system are organized and transformed into the form of differences from their corresponding steady-state values. This approach sets the steady-state operating point of the system as the origin of the state space coordinates. The superscript 0 represents the steady-state value of the system at the initial operating point. For example, ω_{FM}^0 denotes the steady-state value of the GFM converter, and other state variables are represented in such similar manner. And the specific expression is given by

$$\begin{cases} x_1 = \omega_{FM} - \omega_{FM}^0 & x_2 = u_{cd}^{FM} - u_{cd}^{FM0} \\ x_3 = u_{cq}^{FM} - u_{cq}^{FM0} & x_4 = i_d^{FM} - i_d^{FM0} \\ x_5 = i_q^{FM} - i_q^{FM0} & x_6 = \omega_{FL} - \omega_{FL}^0 \\ x_7 = u_{cd}^{FL} - u_{cd}^{FL0} & x_8 = u_{cq}^{FL} - u_{cq}^{FL0} \\ x_9 = i_d^{FL} - i_d^{FL0} & x_{10} = i_q^{FL} - i_q^{FL0} \\ x_{11} = v_{dc}^{FL} - v_{dcref}^{FL} & x_{12} = Q^{FL} - Q_{ref}^{FL} \\ x_{13} = i_{gd}^{FM} - i_{gd}^{FM0} & x_{14} = i_{gq}^{FM} - i_{gq}^{FM0} \\ x_{15} = u_d^{ML} - u_d^{ML0} & x_{16} = u_q^{ML} - u_q^{ML0} \\ x_{17} = s_{ud}^{ML} - s_{ud}^{ML0} & x_{18} = s_{uq}^{ML} - s_{uq}^{ML0} \\ x_{19} = \omega_{MI} - \omega_{MI}^0 & x_{20} = s_{PLL}^{MI} - s_{PLL}^{MI0} \\ x_{21} = i_d^{MI} - i_d^{MI0} & x_{22} = i_q^{MI} - i_q^{MI0} \\ x_{23} = \sin\theta_{MI} - \sin\theta_{MI}^0 & x_{24} = \cos\theta_{MI} - \cos\theta_{MI}^0 \\ x_{25} = s_{dc}^{MI} - s_{sc}^{MI0} & x_{26} = s_Q^{MI} - s_Q^{MI} \\ x_{27} = i_{gd}^{ML} - i_{gd}^{ML0} & x_{28} = i_{gq}^{ML} - i_{gq}^{ML0}. \end{cases} \tag{11}$$

Furthermore, the dynamic model of the system can be specifically introduced in (12) and the rest of the complex formulas

are on the last page of this article.

$$\begin{cases} \dot{x}_3 = \left(x_2 + u_{cd}^{FM0}\right) x_1 \quad \dot{x}_4 = -\left(x_5 + i_q^{FM0}\right) x_1 \\ \dot{x}_5 = \left(x_4 + i_q^{FM0}\right) x_1 \quad \dot{x}_6 = k_p^{FLP} x_8 + k_i^{FLP} x_{14} \\ \dot{x}_7 = \left(\omega_{FL}^0 C_{FL} x_8 + x_9 - x_{15}\right) / C_{FL} \\ \dot{x}_8 = \left(-\omega_{FL}^0 C_{FL} x_7 + x_{10} - x_{16}\right) / C_{FL} \\ \dot{x}_9 = -\left(x_{10} + i_q^{FL0}\right) x_6 \quad \dot{x}_{10} = \left(x_9 + i_d^{FL0}\right) x_6 \\ \dot{x}_{11} = -x_{12} / \left[C_{dc}^{FL}\left(x_{11} + v_{dc}^{FL0}\right)\right] \\ \dot{x}_{15} = \left(-k_p^{ML} x_{15} + k_i^{ML} x_{17}\right) / C_g^{ML} \\ \dot{x}_{16} = \left(-k_p^{ML} x_{16} + k_i^{ML} x_{18}\right) / C_g^{ML} \\ \dot{x}_{17} = -x_{15} \quad \dot{x}_{18} = -x_{16} \quad \dot{x}_{20} = x_{22} + u_q^{MI0} \\ \dot{x}_{21} = -\left(x_{22} + i_q^{MI0}\right) x_{19} \quad \dot{x}_{22} = \left(x_{21} + i_d^{MI0}\right) x_{19} \\ \dot{x}_{23} = \left(x_{24} + \cos\theta_{MI}^0\right) x_{19} \quad \dot{x}_{24} = -\left(x_{23} + \sin\theta_{MI}^0\right) x_{19} \\ \dot{x}_{25} = k_i^{MI}\left(x_{21} - 3x_{25}\right) / 3k_p^{MI} \\ \dot{x}_{26} = k_i^{MI}\left(x_{22} - 3x_{26}\right) / 3k_p^{MI}. \end{cases} \tag{12}$$

Comprehensive analysis of the aforementioned state-space expressions reveals that the system is characterized by high order, strong nonlinearity, and multifrequency coupling. These features make it challenging to perform large-signal interaction stability analysis using direct methods to construct Lyapunov function. Additionally, the excessive number of nonlinear terms leads to a dimensionality curse for traditional sector nonlinearity methods, such as TS fuzzy and SOS methods.

III. Proposed Fuzzy Tensor Space Method

Based on the characteristics of the dynamic system model described in Section II, improvements to the sector nonlinearity method need to be made in two aspects. First, the number of membership functions should be reduced to address the dimensionality curse. Second, the solution methods should be optimized to reduce the conservativeness of classical solution strategies such as TS fuzzy and SOS. This article integrates both aspects by combining the linear independence of membership function tensors and spatial mapping relationships. The fuzzy tensor space method is proposed to analyze the large-signal stability of complex interactive power electronic converter systems.

A. Dimensionality Curse Solution

The complexity of constructing the system's Lyapunov function based on the sector nonlinearity method primarily arises from the number of nonlinear terms. Therefore, it is essential to first extract all these terms from the dynamic model. The specific forms of the $p = 14$ nonlinear terms are as follows:

$$\begin{cases} g_1(\boldsymbol{x}) = x_1 + \omega_{FM}^0 & g_2(\boldsymbol{x}) = x_2 + u_{cd}^{FM0} \\ g_3(\boldsymbol{x}) = x_3 + \omega_{cq}^{FM0} & g_4(\boldsymbol{x}) = x_4 + i_d^{FM0} \\ g_5(\boldsymbol{x}) = x_5 + i_q^{FM0} & g_6(\boldsymbol{x}) = x_7 + u_{cd}^{FL0} \\ g_7(\boldsymbol{x}) = x_8 + u_{cq}^{FL0} & g_8(\boldsymbol{x}) = x_9 + i_d^{FL0} \\ g_9(\boldsymbol{x}) = x_{10} + i_q^{FL0} & g_{10}(\boldsymbol{x}) = x_{11} + v_{dc}^{FL0} \\ g_{11}(\boldsymbol{x}) = x_{21} + i_d^{MI0} & g_{12}(\boldsymbol{x}) = x_{22} + i_q^{MI0} \\ g_{13}(\boldsymbol{x}) = x_{23} + \sin\theta_{MI}^0 & g_{14}(\boldsymbol{x}) = x_{24} + \cos\theta_{MI}^0 \end{cases}. \tag{13}$$

Due to the high order of the system, it is necessary to establish sectors in the high-dimensional space to cover the regions of each quadrant in order to accurately represent the original nonlinear system. Let each quadrant on the input space be considered as a local region. In each local region, any function can be globally or semiglobally covered by sectors. First, it is necessary to define the quadrants in the high-dimensional space, considering a certain situation

$$x_1 \geqslant 0, x_2 \leqslant 0, x_3 \leqslant 0, x_4 \geqslant 0, \ldots, x_n \geqslant 0. \tag{14}$$

The quadrant R it represents can be defined as

$$R(s_1, s_2, s_3, s_4, \ldots, s_n) \to R(1, 0, 0, 1, \ldots, 1) \tag{15}$$

where $s_1 = 1, s_4, s_5, \ldots, s_n = 1, s_2 = s_3 = 0$ and $s_j = 1(x_j \geqslant 0), s_j = 0(x_j \leqslant 0)$. Using the above definitions, the first and second quadrants in a single-variable system are represented as $R(1)$ and $R(0)$, respectively. In each symmetric quadrant region relative to the origin, a common sector can be used to cover a function. In a two-variable system, the common sector in $R(1,1)$ and $R(0,0)$ can be used for coverage. For regions that combine symmetric quadrants relative to the origin, a common sector can cover the original multivariable nonlinear equation $y = f(\boldsymbol{x})$. Therefore, by extending this to n-dimensional space, the overlapping and coverage relationships of these quadrants can be expressed as the following regions:

$$\begin{cases} R(1,1,1,\ldots,1,1,1) \cup R(0,0,0,\ldots,0,0,0) \\ R(0,1,1,\ldots,1,1,1) \cup R(1,0,0,\ldots,0,0,0) \\ R(1,0,1,\ldots,1,1,1) \cup R(0,1,0,\ldots,0,0,0) \\ R(1,1,0,\ldots,1,1,1) \cup R(0,0,1,\ldots,0,0,0) \\ \qquad\qquad \vdots \\ R(0,0,0,\ldots,0,0,1) \cup R(1,1,1,\ldots,1,1,0) \end{cases} \tag{16}$$

where the total number of regions is $Q = 2^{n-1}$, and R^* is defined as the symmetric quadrant of R. Next, in the multivariable high-dimensional space, some constraints need to be assumed in order to uniquely construct a multidimensional sector. Suppose a region p that satisfies

$$R(s_1, \ldots, s_{p-1}, s_p, \ldots, s_n) \cup R^*(s_1, \ldots, s_{p-1}, s_p, \ldots, s_n) \tag{17}$$

where $s_1, \ldots, s_{p-1} = 0, s_p, \ldots, s_n = 1$. After performing first-order differentiation on the variables of the original multivariable nonlinear equation, the maximum and minimum values in the region p can be found as

$$\begin{cases} \bar{a}_{1p} = \max\limits_{x_1,\ldots,x_n} \frac{\partial f}{\partial x_1} & \underline{a}_{1p} = \min\limits_{x_1,\ldots,x_n} \frac{\partial f}{\partial x_1} \\ \bar{a}_{2p} = \max\limits_{x_1,\ldots,x_n} \frac{\partial f}{\partial x_2} & \underline{a}_{2p} = \min\limits_{x_1,\ldots,x_n} \frac{\partial f}{\partial x_2} \\ \qquad\vdots & \qquad\vdots \\ \bar{a}_{np} = \max\limits_{x_1,\ldots,x_n} \frac{\partial f}{\partial x_n} & \underline{a}_{np} = \min\limits_{x_1,\ldots,x_n} \frac{\partial f}{\partial x_n}. \end{cases} \tag{18}$$

On the basis of the extension of high-dimensional sector nonlinear method, its theory can be applied to the specific analysis of large signal stability in multipower electronic device interaction system. Assuming that the values of these nonlinear terms lie within a bounded compact set, they can be represented as follows:

$$\underline{g}_k \leq g_k(\boldsymbol{x}) \leq \bar{g}_k \ (\forall k \in \{1, 2, \ldots, p\}). \tag{19}$$

Therefore, the membership function $h_q(g)$ can be represented as follows:

$$\begin{cases} G_k^{\bar{\sigma}}(g_k) = \frac{\bar{g}_k - g_k}{\bar{g}_k - \underline{g}_k},\ G_k^{\underline{\sigma}}(g_k) = \frac{g_k - \underline{g}_k}{\bar{g}_k - \underline{g}_k} \\ H_q(g) = G_k^{\sigma}(g_k) / \sum \prod_{k=1}^{p} G_k^{\sigma}(g_k),\ \sum_{q=1}^{r} H_q(g) = 1. \end{cases} \tag{20}$$

Then, high-dimensional sectors can be constructed based on the extreme values of the system's nonlinear terms, and the corresponding membership functions possess normalization and standardization properties, which comply with the application conditions of the sector nonlinear method.

Specifically, based on the aforementioned $p = 14$ nonlinear terms, the system's TS fuzzy rules consist of $r = 2^{14} = 16384$ rules, each corresponding to a different local linear fuzzy model formed by the permutations and combinations of the extreme values of the nonlinear terms. The system matrix of the fuzzy model can be defined as X_q, and the specific expression of the fuzzy rules is as follows:

1) *Fuzzy Rule 1:* if $g_1(\boldsymbol{x}) = \underline{g}_1 = \underline{x}_1 + \omega_{FM}^0$, $g_2(\boldsymbol{x}) = \underline{g}_2$, $\cdots, g_{14}(\boldsymbol{x}) = \underline{g}_{14}$, the local system fuzzy matrix $X_1(\underline{g}_1, \underline{g}_2, \ldots, \underline{g}_{14})$ could describe the system as $\dot{\boldsymbol{x}}(t) = f(\boldsymbol{x}) = X_1\boldsymbol{x}$.

2) *Fuzzy Rule 2:* if $g_1(\boldsymbol{x}) = \underline{g}_1$, $g_2(\boldsymbol{x}) = \bar{g}_2, \cdots, g_{14}(\boldsymbol{x}) = \underline{g}_{14}$, the local system fuzzy matrix $X_2(\underline{g}_1, \bar{g}_2, \ldots, \underline{g}_{14})$ could describe the system as $\dot{\boldsymbol{x}}(t) = f(\boldsymbol{x}) = X_2\boldsymbol{x}$.

$\cdots\ \cdots$

r) *Fuzzy Rule r:* if $g_1(\boldsymbol{x}) = \bar{g}_1$, $g_2(\boldsymbol{x}) = \bar{g}_2, \cdots, g_{14}(\boldsymbol{x}) = \bar{g}_{14}$, the local system fuzzy matrix $X_r(\bar{g}_1, \bar{g}_2, \ldots, \underline{g}_{14})$ could describe the system as $\dot{\boldsymbol{x}}(t) = f(\boldsymbol{x}) = X_r\boldsymbol{x}$.

Finally, the dynamic model of the entire system can be expressed by the TS fuzzy model as

$$\dot{\boldsymbol{x}}(t) = f(\boldsymbol{x}) = \sum_{q=1}^{r} H_q(g) X_q \boldsymbol{x}(t)\ \ (r = 2^p) \tag{21}$$

where the membership functions $H_q(g)$ is described by the subordinate equations named $G_k^{\sigma}(g_k)$, the specific form can be expressed as

$$\begin{aligned} G_1^{\sigma}(g_k) = &\frac{g_1(\boldsymbol{x}) - \underline{g}_1(\boldsymbol{x})}{\bar{g}_1(\boldsymbol{x}) - \underline{g}_1(\boldsymbol{x})} \times \frac{g_2(\boldsymbol{x}) - \underline{g}_2(\boldsymbol{x})}{\bar{g}_2(\boldsymbol{x}) - \underline{g}_2(\boldsymbol{x})} \\ &\times \cdots \times \frac{g_{14}(\boldsymbol{x}) - \underline{g}_{14}(\boldsymbol{x})}{\bar{g}_{14}(\boldsymbol{x}) - \underline{g}_{14}(\boldsymbol{x})} \end{aligned} \tag{22}$$

$$\begin{aligned} G_r^{\sigma}(g_k) = &\frac{g_1(\boldsymbol{x}) - \bar{g}_1(\boldsymbol{x})}{\bar{g}_1(\boldsymbol{x}) - \underline{g}_1(\boldsymbol{x})} \times \frac{g_2(\boldsymbol{x}) - \bar{g}_2(\boldsymbol{x})}{\bar{g}_2(\boldsymbol{x}) - \underline{g}_2(\boldsymbol{x})} \\ &\times \cdots \times \frac{g_{14}(\boldsymbol{x}) - \bar{g}_{14}(\boldsymbol{x})}{\bar{g}_{14}(\boldsymbol{x}) - \underline{g}_{14}(\boldsymbol{x})}. \end{aligned} \tag{23}$$

Thus, the membership functions $H_q(g)$ can be calculated as

$$\begin{aligned} &H_1(g) = G_1^{\sigma}(g_k) / \sum_{k=1}^{r} G_k^{\sigma}(g_k) \cdots \\ &\Rightarrow H_r(g) = G_r^{\sigma}(g_k) / \sum_{k=1}^{r} G_k^{\sigma}(g_k). \end{aligned} \tag{24}$$

Based on (21), in the simplest case, the number of fuzzy rules will reach $2^{14} = 16384$, which increases exponentially with the number of nonlinear terms. It presents significant challenges in solving the Lyapunov function and DOA for the entire complex system. To simplify the complexity of the membership functions, by observing (20), it is evident that all membership functions are a series of combinations formed by the extreme values of the nonlinear terms. In addition, there exists information redundancy, meaning that only a subset of membership functions is required to represent the remaining ones. Without loss of generality, it can be summarized that in the membership function space, it is necessary to find a set of basis tensors that can represent the entire space with the fewest membership function tensors. Using mathematical induction, the general relationship among the tensors in the membership function space is summarized as follows:

$$X_i = X_{2^p-1} - X_{2^{p-1}-1} + X_{i-2^{p-1}} \tag{25}$$

where $2 \le p \le r,\ 1 + 2^{p-1} \le i \le 2^p$ (there is a detailed case in Appendix A). Therefore, a set $\mathscr{X} = \{1, 2, 3, 7, \ldots, 2^p - 1\}$ of membership function tensor bases can be defined. It allows the original complex nonlinear system to be re-expressed by identifying the corresponding $(p+1)$ membership functions and local linear matrices from the original TS fuzzy expressions, which is as follows:

$$\dot{\boldsymbol{x}}(t) = f(\boldsymbol{x}) = \sum \mathscr{H}_q(g) X_q \boldsymbol{x}(t)\ \ (q \in \mathscr{X}). \tag{26}$$

Subsequently, to further obtain the specific expression of the new membership function tensor bases corresponding to (26), two new sets, $\mathscr{I}_j^+(r)$ and $\mathscr{I}_j^-(r)$, need to be defined, with the subscript $j \in \mathscr{J}_r = \{2^p - 1 : p \in \mathscr{X}\} \cup \{2\}$. For different conditions of the set parameters, the relationship between the two sets and the membership function tensors in (25) can be derived. Firstly, if $l < p$, then the specific expression is

$$\begin{cases} \mathscr{I}_j^+(l) = \mathscr{I}_j^-(l) = \oslash,\ \mathscr{I}_j^+(p+1) = \mathscr{I}_j^+(p) \\ \mathscr{I}_j^+(p) = \left\{i : 1 + 2^{p+1} \le i \le 2^p\right\},\ \mathscr{I}_j^-(k) = \oslash \\ \mathscr{I}_j^-(p+1) = \left\{i : 1 + 2^{p+1} \le i \le 2^{p-1} + 2^p\right\}. \end{cases} \tag{27}$$

Second, if $l \ge p+2$ and $2 \le p \le r-1$, the relationship with $\Delta = i + 2^{p+1}(k-1)$ would be

$$\begin{cases} \mathscr{I}_j^+(r) = \left\{\Delta : 1 + 2^{p-1} \le i \le 2^p, 1 \le k \le 2^{r-p-1}\right\} \\ \mathscr{I}_j^-(r) = \left\{\Delta : 1 + 2^p \le i \le 2^{p-1} + 2^p, 1 \le k \le 2^{r-p-1}\right\}. \end{cases} \tag{28}$$

Thus, for $p \ge 2$, the new membership function tensor bases can be rewritten as

$$\begin{cases} \mathscr{H}_1 = \sum_{j=1}^{2^{p-2}} H_{4j-3} - \sum_{j=1}^{2^{p-2}} H_{4j}, \mathscr{H}_2 = \sum_{j=1}^{2^{p-1}} H_{2j} \\ \mathscr{H}_{2^p-1} = \sum_{j=1+2^{p-1}}^{2^p} H_j, \mathscr{H}_{2^{k-1}} = \Psi(H)\ (k \in \mathscr{X} \backslash \{1\}) \end{cases} \tag{29}$$

where defining $\sigma = i + (j-1)2^{k+1}$ the detailed expression of $\Psi(H)$ is

$$\Psi(H) = \sum_{j=1}^{2^{r-k-1}} \left(\sum_{i=1+2^{k-1}}^{2^k} H_\sigma - \sum_{i=2^k+1}^{2^{k-1}+2^k} H_\sigma \right). \tag{30}$$

Moreover, all the membership function tensor bases would satisfy

$$-1 \leq \mathscr{H}_q(g) \leq 1, \ \sum_{q\in\mathscr{X}} \mathscr{H}_q(g) = 1. \tag{31}$$

Since the value range of the membership function tensor bases in (31) includes negative values, the entire space is not convex. By defining the new tensor form as follows:

$$\begin{cases} \tilde{H}_2 = \mathscr{H}_2, \tilde{H}_p = \mathscr{H}_p \\ \tilde{H}_k = \mathscr{H}_k + 1 \, (k \in \mathscr{X} \backslash \{2, 2^p - 1\}) \end{cases} \tag{32}$$

and the membership tensor fuzzy model of the entire system with $(p+1)$ normalized tensor basis can be obtained as

$$\begin{cases} \dot{\boldsymbol{x}}(t) = \sum \tilde{H}_q(g) X_q \boldsymbol{x}(t) \ \ (q \in \mathscr{X} \cup \{0\}) \\ -X_0 = \sum_{j\in\mathscr{X}\backslash\{2,2^p-1\}} X_j, \ \tilde{H}_0 = 1 \end{cases} \tag{33}$$

In summary, by leveraging the linear independence of tensor bases in the fuzzy tensor space, the dimensionality curse of complex systems is addressed. This approach reduces the complexity from an exponential order 2^p to a constant level $(p+1)$.

B. Lyapunov Conservativeness Optimization

Define a quadratic Lyapunov function $V = \boldsymbol{x}^T \mathbb{B} \boldsymbol{x}$. Using (33) and the Lyapunov inequality, the conditions for solving the positive definite symmetric matrix $\mathbb{B}$ and matrix $\mathscr{Q}$ are given by

$$\begin{cases} X_0^T \mathbb{B} + \mathbb{B} X_0 - \mathscr{Q} < 0 \\ X_q^T \mathbb{B} + \mathbb{B} X_q + \mathscr{Q}/p < 0, \ (q \in \mathscr{X}) \, . \end{cases} \tag{34}$$

Furthermore, if the conditions in (34) are used to construct an auxiliary convex optimization problem for solving the Lyapunov function using traditional TS fuzzy theory method, the resulting conservativeness will be excessively high due to the lack of dependence on the membership function tensors.

Therefore, to enhance the accuracy, it is necessary to analyze the membership function tensors and their spatial physical significance. As shown in Fig. 4(a), using a 2-D fuzzy tensor space as an example, the values of the two tensor bases range between 0 and 1, with a maximum value of 1, represented by the black line in the figure. Furthermore, since the sum of the tensor bases is constant, as the black line progressively moves inward toward the blue and red lines, the region corresponding to the Lyapunov inequality's tensor space expands. It can be concluded that there is an inverse correlation between the region determined by the fuzzy tensors and the Lyapunov attraction domain. This means that reducing the fuzzy tensor region can decrease the conservativeness of the Lyapunov function solution. Thus, the two extreme values of the fuzzy tensor are defined as follows:

$$\tilde{H}_i^{\min} \triangleq \min_{\boldsymbol{x}} \left\{ \tilde{H}_i(\boldsymbol{x}) \right\} \quad \tilde{H}_i^{\max} \triangleq \max_{\boldsymbol{x}} \left\{ \tilde{H}_i(\boldsymbol{x}) \right\}. \tag{35}$$

Then, Fig. 4(b) illustrates a method for reducing the region in a 3-D tensor space based on the extreme values of the fuzzy tensor. Based on the geometric analysis in this vector space, if the LMI constraint conditions in the Lyapunov equation are mapped to some points in the fuzzy tensor space, the convex

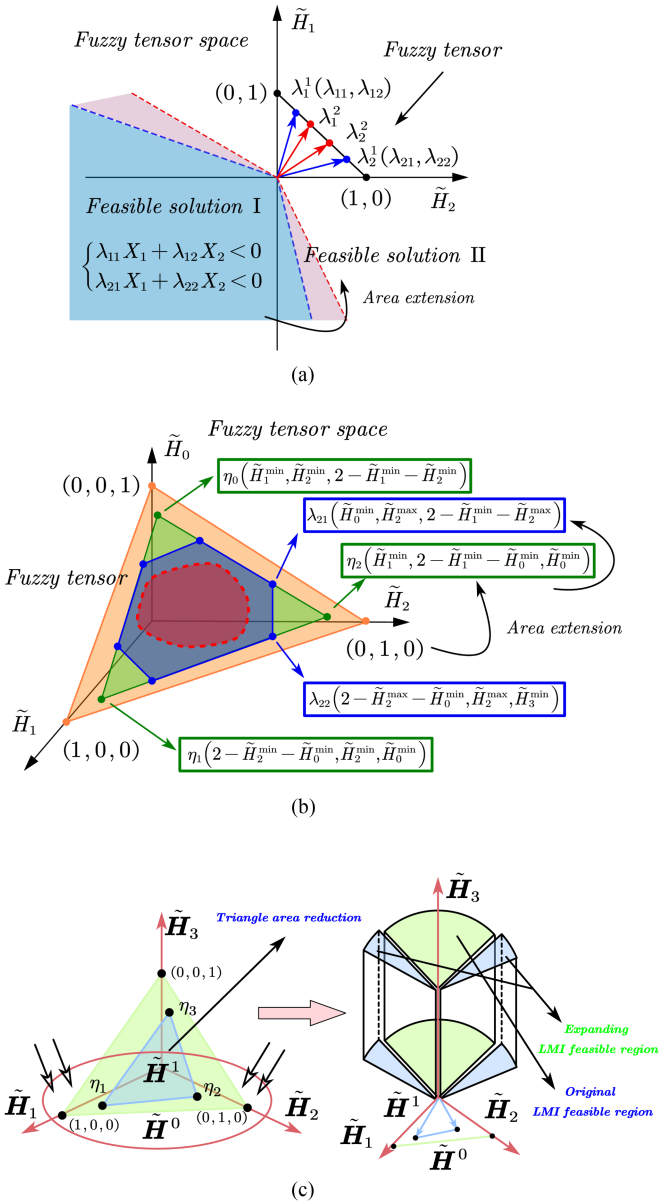

Fig. 4. Physical significance for fuzzy tensors and tensor space in different dimensional spaces. (a) 1-D fuzzy tensor space. (b) 2-D fuzzy tensor space. (c) 2-D fuzzy tensor space and its conservative geometric meaning.

polytope constructed by these points will indicate the conservatism of the system's stability result. Let the standard basis of the d-dimensional Euclidean space be $(e_1, e_2, \ldots, e_d)$. If the constraints in the LMI problem framework are satisfied, it means that the system described by the matrix corresponding to the fuzzy tensor mapped from any point within the convex polytope with vertices at e_j is stable. These convex polytopes can be viewed as the mapping of the fuzzy tensor in the membership function space. Specifically, if the trajectory of $\boldsymbol{H}$ is constrained within the convex polytope, the system $\sum_{j=1}^{d} \boldsymbol{H}_j \boldsymbol{A}_j$ will be large-signal stable. Furthermore, we need to analyze how to reduce the conservatism of the solution by shrinking the generalized area of the polytope represented by $(e_1, e_2, \ldots, e_d)$.

As shown in Fig. 4(c), in 3-D space, when the convex region represented by the standard basis with vertices at $(1,0,0)$, $(0,1,0)$, and $(0,0,1)$ is reduced to a triangle with vertices at η_j, it is clear that the reduction in the triangle's area corresponds exactly to the feasible domain of the LMI. In this special case, the triangular region can be viewed as a mapping of the conservatism of the solution in the membership function space.

Without loss of generality, this method can be extended to higher-dimensional tensor spaces with the vertices calculation as follows. First, define a new class of fuzzy tensors as $\bar{H}$, with a minimum value of 0 and a maximum value represented as

$$\alpha_{qk} = \bar{H}^{\max}_{(q+k)p} = \left(\tilde{H}^{\max}_{(q+k)p} - \tilde{H}^{\min}_{(q+k)p}\right)/\delta \tag{36}$$

where $\delta \triangleq 2 - \sum \tilde{H}^{\min}_i$ and $q \in \mathscr{X} \cup \{0\}$, $k \in \mathscr{X}$. Subsequently, make some corresponding variables as $\beta_{qm0} = \alpha_{q0}$ and $\beta_{qmk} = \alpha_{q(m+k-1)_{p-1}}$ for all $q \in \mathscr{X} \cup \{0\}$, $m, k \in \mathscr{X}$. Then, after setting $k = 1$, the condition in (37) should be checked whether it is satisfied or not

$$\beta_{qmk} > 1 - \sum_{i=0}^{k-1} \beta_{qmi}. \tag{37}$$

There are two possible outcomes here. If the condition is not met, set $k = k + 1$ and repeat the above inspection steps. If the condition is met, change the inequality to an equality for assignment.

At last, defining three new variables as

$$\gamma_{qmk} = \beta_{qm(k-m+1)_{p-1}} \Rightarrow \tilde{\lambda}_{qmk} = \gamma_{qm[k-q]_p} \tag{38}$$

where the proposed calculation function can be expressed by $[a]_b \triangleq a \bmod b$, and the vertices for the final fuzzy tensor region can be calculated as

$$\lambda_{qmk} = \delta\tilde{\lambda}_{qmk} + \tilde{H}^{\min}_k \Rightarrow \lambda_{qm} = (\lambda_{qm0}, \lambda_{qm1}, \ldots, \lambda_{qmp}). \tag{39}$$

As a result, to avoid the increased conservativeness that could arise from reducing the number of membership functions, the fuzzy tensor space method is employed to enhance the accuracy of the Lyapunov solution. Ultimately, this approach improves the analysis theory for large-signal interaction stability in complex power electronic systems from both the complexity and accuracy parts.

Specifically, the improvements and optimization steps for typical methods can be illustrated in Fig. 5. The final Lyapunov function and its corresponding critical energy V_c represent the attraction domain of the entire system in a 28-D space, which is a hypersphere and difficult to describe and analyze intuitively. To facilitate quantitative analysis of the system's stability results, the attraction domain can be projected onto a specific 2-D plane, resulting in an elliptical form. It is important to note that the selection of the 2-D plane should follow two principles: 1) the state variables most relevant to large signal disturbances, which can represent the system's transient process in the state trajectory; 2) the plane that best reflects the differences in the attraction domain under different conditions, based on the system stability mechanism under focus. In the subsequent analysis of the system's attraction domain results, the aforementioned projection and principles can be applied to clearly and intuitively reveal the system's stability mechanism.

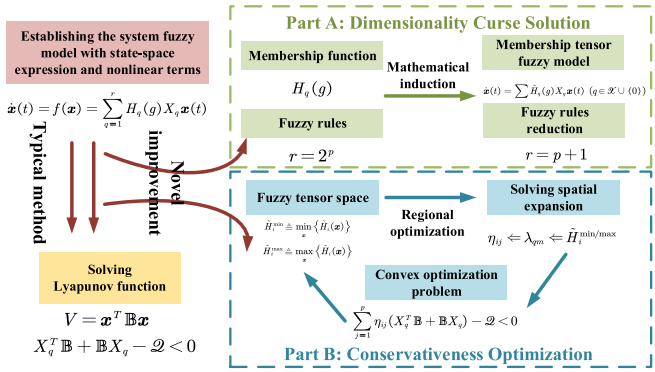

Fig. 5. Improvements and optimization steps for typical methods.

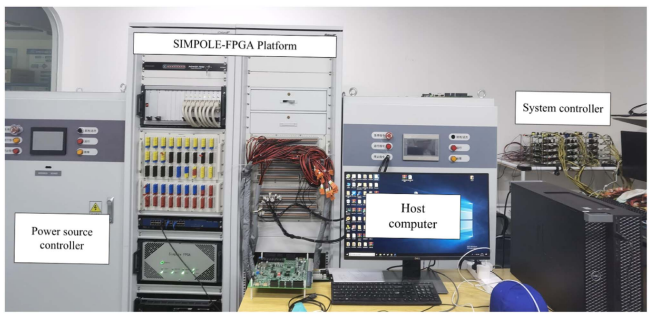

Fig. 6. Hybrid system experimental platform.

IV. Theoretical Analysis and Experimental and Simulation Results

Theoretical analysis and experimental results are used to validate the effectiveness of the large-signal stability analysis of the interactions between M3C and grid-connected converters with GFM/GFL hybrid control strategies. The system undergoes testing through a Control-Hardware-in-the-Loop simulation platform, specifically using the SIMPOLE-FPGA Platform with the XC7VX690T-FPGA. Fig. 6 illustrates the experimental platform, with the experimental parameters aligned with the simulation parameters detailed in Table I.

A. Identical Mixing Ratio of GFM/GFL Converters

Firstly, the transmission power ratio of the GFM converter to the GFL converter is defined as the mixing ratio R, representing different operating conditions in their interaction with M3C. Under the condition of $R = 1$, considering significant disturbances in the power fluctuations of grid-connected converters, the terminal operating point T_1 ($P = 1.50$ p.u.) and two different initial operating points O_1 ($P = 0.83$ p.u.) and O_2 ($P = 0.50$ p.u.). Furthermore, various methods are employed to solve the system's attraction domain and project it into 2-D space for analysis, as shown in Fig. 7. To facilitate comparison and analysis, the target operating point T_1 is affinely transformed

TABLE I
PARAMETERS VALUES HYBRID SYSTEM

System	Description	Value
Base Parameter	Base power	5MW
	Base voltage	3.3kV
	Base angular velocity	100πrad/s
Hybrid Converters	Signal turbine rated capacity	2.5MW
	Active power virtual inertia J	2.5×10^5
	Virtual damping D	2.5×10^6
	Reactive power virtual inertia Λ	1×10^4
	Outer loop control parameter k_{pi}^{FL}	2/20
	PLL control parameter k_{pi}^{FLP}	0.1/10
M3C	Bridge arm inductance L_M	30mH
	Filter capacitor C_g^{ML}	200μF
	LF outer loop control parameter k_{pi}^{ML}	0.1/5
	HF outer loop control parameter k_{pi}^{MI}	1/10
	HF PLL control parameter k_{pi}^{MIP}	0.2/10

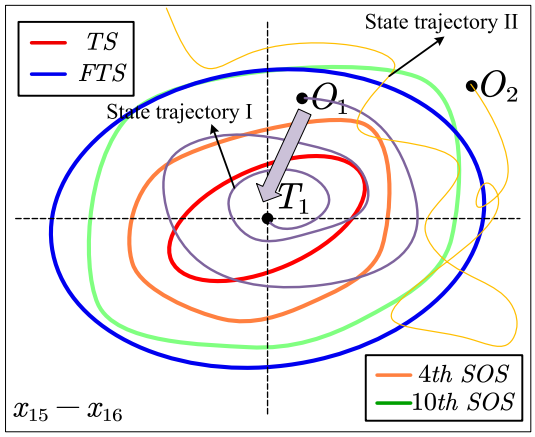

Fig. 7. Comparison of results for solving the attraction domain using various methods with $R = 1$.

to the coordinate origin. The attractor domains corresponding to T_1 solved by different methods are described by different colored curves in Fig. 7. In the projection plane corresponding to $x_{15} - x_{16}$, the state variables corresponding to O_1 and O_2 will also have mappings in this plane. Thus, the system's operating conditions under large signal disturbances can be described as the process of transitioning from the initial operating points O_1 and O_2 towards the target operating point T_1 in the plane. The corresponding state trajectories in Fig. 7 also start from the initial operating points, with the trajectories they follow representing new system states different from the initial state, i.e., the transient process, until they reach the new equilibrium state at the target operating point T_1, or diverge due to system instability.

The T_1 at the coordinate origin corresponds to the attraction domains obtained by four different methods, where FTS denotes the Fuzzy Tensor Space method proposed in this article. From a conservative viewpoint, the traditional TS method is overly conservative for high-order nonlinear problems, whereas the conservativeness of the SOS method decreases with the increasing order of the Lyapunov function. Additionally, the computational region of the 10th-order SOS method aligns closely with the proposed method, which is 42% larger than

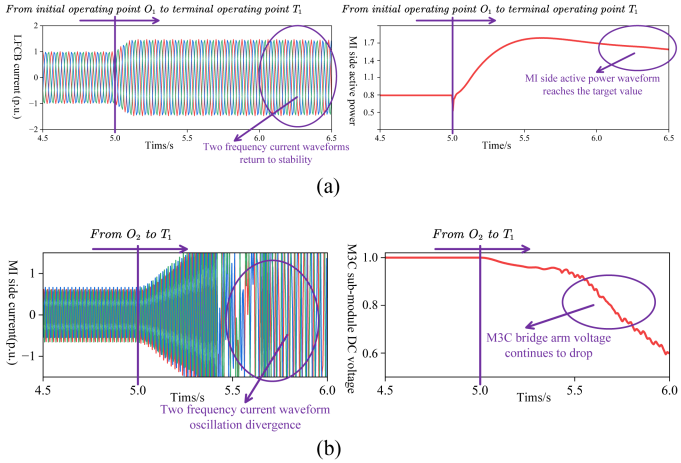

Fig. 8. Transient simulation waveform results of the system transitioning from O_1 and O_2 to T_1. (a) The transient process from O_1 to T_1. (b) The transient process from O_2 to T_1.

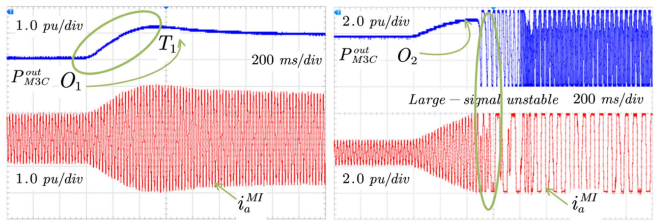

Fig. 9. Transient experimental waveform results of the system transitioning from O_1 and O_2 to T_1.

the traditional methods. Then, from the analysis of the results for state trajectory I and state trajectory II corresponding to O_1 and O_2 in Fig. 7, it can be observed that state trajectory I gradually converges to the equilibrium origin after starting from the initial operating point. In contrast, state trajectory II follows a relatively chaotic transient process before eventually diverging and leaving the coordinate range of Fig. 7. By considering the relative position relationship between the initial equilibrium point and the corresponding attractor domain, and based on the Lyapunov stability criterion, the equilibrium state of the system after different large-signal disturbances can be determined.

In Figs. 8 and 9, the cases corresponding to two different initial operating points, O_1 and O_2, illustrating the transient response to large-signal disturbances through the simulation and experimental waveform of the M3C output power P_{M3C}^{out} and the a-phase current i_a^{MI} on the ML side. When transitioning from O_1 to T_1, both the power and current of the M3C return to the target stable state after a period of transience, indicating that the system maintains large-signal stability. Furthermore, the analysis results using the attraction domain theory in Fig. 7 demonstrate that the TS and lower-order SOS methods provide overly conservative results, leading to inaccuracies. In contrast, the proposed method, along with the 10th-order SOS, offers superior accuracy in large-signal stability analysis. Similarly, the large-signal stability at O_2 is validated, aligning with the analysis

TABLE II
COMPARATIVE ANALYSIS

	Time	Efficiency	Order
TS	357.91s	2^p	2
4th SOS	802.35s	p^4	4
10th SOS	1832.71s	p^{10}	10
FTS	632.12s	$p(p+1)$	2

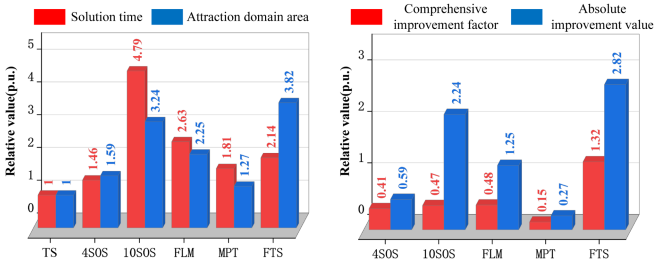

Fig. 10. Comprehensive quantitative analysis of the various analysis methods.

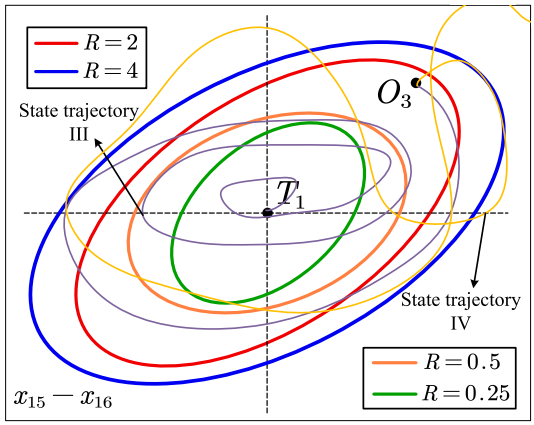

Fig. 11. Comparison of results for solving the attraction domain using various mixing ratio R.

results of each attraction domain. However, the final waveform divergence at O_2 indicates the onset of large-signal instability. These simulation and experimental results robustly confirm the proposed method's advantage in addressing the conservatism inherent in traditional methods.

On the other hand, in terms of computational complexity, calculations are performed using the computer equipped with an Octa-Core Intel i9 processor and 16 GB of memory. From the analysis in Table II, it can be seen that although the FTS method took twice as long as the TS method, it is nearly five times more efficient than the high-order SOS algorithm while maintaining lower conservativeness. Furthermore, it compared the proposed improved method, FTS, with classical TS fuzzy theory (TS), 4th-order SOS (4SOS), 10th-order SOS (10SOS), Mixed Potential Theory (MPT), and Fuzzy Lyapunov Method (FLM), conducting a quantitative analysis of their differences in computation time reduction and attraction domain area expansion. The results are shown in Fig. 10. Using the results obtained by TS as the baseline, the results of other methods were normalized, and the attraction domain area difference from the TS baseline value of 1 was defined as the absolute improvement value. The ratio of this difference to the computation time was taken as the comprehensive improvement coefficient. Taking the TS solution time of 357.91 s as the standard, the 10th-order SOS method has a much higher solution order, nearly seven times more complex than the FTS method, yet it also shows significant improvement in conservatism. The proposed optimization method is the most optimal in terms of conservatism improvement, with a solution speed 2.14 times that of the classical methods, similar to the time consumption of FLM and MPT methods. However, as concluded from earlier theoretical analysis, complexity and accuracy are complementary concepts that need to be analyzed comprehensively. In terms of the comprehensive improvement coefficient, only the proposed method exceeds 1, indicating that after considering both aspects, it has a positive impact on the overall large-signal stability of the system. Compared to the 10th-order SOS method, FTS demonstrates an exponential simplification in solution time due to the fuzzy vector, while maintaining the inclusion of membership function information in the LMI constraints to reduce conservatism. The increase in complexity is still acceptable, and compared to other methods like MPT and 4th-order SOS, the positive impact outweighs the negative. Therefore, the numerical results verify the effectiveness of the proposed improved TS fuzzy large-signal stability method.

In summary, the FTS method reduces the exponential complexity of the nonlinear terms present in TS and SOS methods to a constant level, significantly improving computational efficiency while ensuring reduced conservativeness.

B. *Different Mixing Ratio of GFM/GFL Converters*

To analyze the impact of different converter ratios on large-signal stability under various control strategies, Fig. 11 presents the attraction domain results for four distinct values of R. The results clearly indicate that a higher converter power ratio under the GFM control strategy leads to a larger attraction domain and a higher stability threshold for power fluctuation disturbances. In Fig. 11, O_3 ($P = 0.94p.u$) is selected as the new initial operating point to transition to the same point T_1. The position of O_3 lies exactly outside the attractor domain corresponding to $R = 0.5$, while it is inside the attractor domain corresponding to $R = 4$. Based on the Lyapunov stability criterion, the system at the former is large-signal stable, while the latter will become unstable. State trajectory III and state trajectory IV, shown in Fig. 11, validate the effectiveness of the above theoretical analysis. From a stability mechanism perspective, in a system with a higher proportion of mixed GFM control strategy converters, the active support capability provided by virtual synchronous machine control, under power fluctuation disturbances, can more effectively expand the system's stability margin compared to GFL.

In the simulation and experimental waveforms shown in Figs. 12 and 13, unlike the experiment in Fig. 9, this study uses two different mixed ratios, $R = 4$ and $R = 0.5$, for comparison.

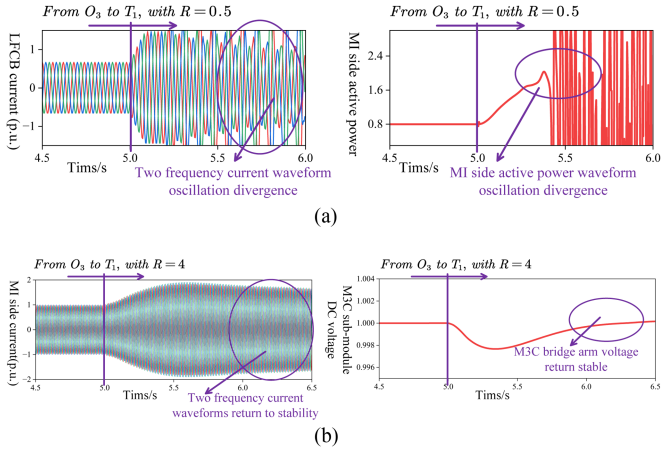

Fig. 12. Transient simulation waveform results of the system transitioning from O_3 to T_1 with various R. (a) The transient process from O_3 to T_1 with $R=0.5$. (b) The transient process from O_3 to T_1 with $R=4$.

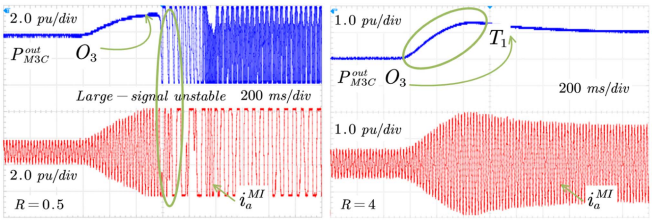

Fig. 13. Transient experimental waveform results of the system transitioning from O_3 to T_1 with various R.

In the simulation waveform shown in Fig. 12(a), when the system transitions from O_3 to T_1 under the condition of $R=0.5$ at 5.0 s, both the low-frequency current of the LFCB and the frequency current of the MI side oscillate and diverge. Meanwhile, the active power waveform of the MI side directly reveals that under the power fluctuation condition, the system fails to maintain dynamic balance and becomes unstable. In contrast, when the system is adjusted to the condition $R=4$ for a similar transient transition, the simulation waveform of Fig. 12(b) shows different results. The current on the MI side stabilizes after a brief transient fluctuation, and it can be reasonably inferred that the low-frequency current follows the same pattern. In addition, the dc voltage of the M3C bridge arm submodule's capacitor stabilizes after a period of fluctuation, indicating that the system can eventually restore power balance and achieve a stable state. The experimental waveforms in Fig. 13 also reveal the same result from the M3C output power and phase-a waveform.

In conclusion, the simulation and experimental results both indicate that under large-signal disturbances of the same intensity, a higher proportion of GFM converter power significantly increases the system's stability threshold, thereby improving the system's safety and reliability. This consistency between experimental results and theoretical analysis confirms the effectiveness of the proposed approach.

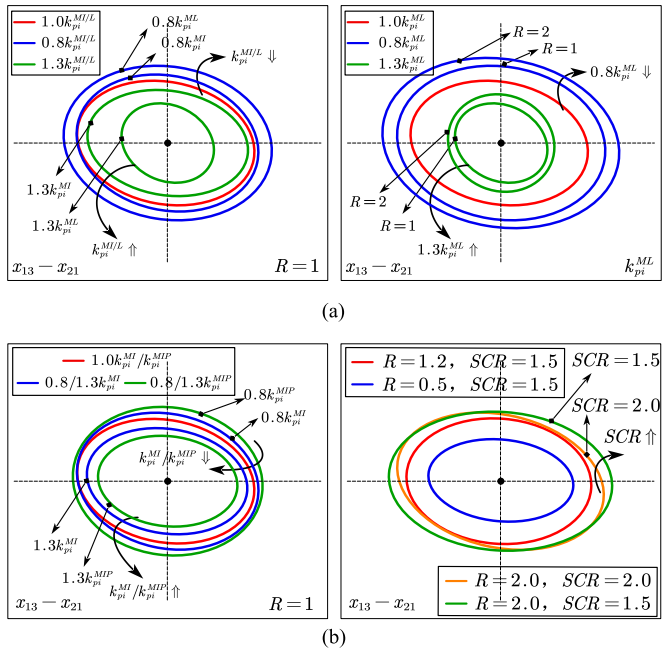

Fig. 14. Comparison of the influence of different aspects of interfrequency interaction characteristics on the attraction domain. (a) M3C outer control parameters from different frequency side. (b) MI side's PLL control parameters and SCR.

C. Interfrequency Interaction Characteristics of M3C

As the core frequency conversion device, the M3C primarily affects the system's interaction stability through interfrequency interaction characteristics. It can be analyzed from two aspects: 1) control parameters on the ML and MI sides; and 2) the SCR corresponding to the LFCB and the ML side of M3C. The analysis of the large signal stability mechanism for the interaction of multiple power electronic devices is an important reference for the design and parameter optimization of converter devices, and it has strong practical significance. However, if classical TS fuzzy theory is used for analysis, the system complexity caused by the mixing of GFL/GFM converters may lead to reduced analysis efficiency. In particular, regarding computational accuracy, overly conservative attractor domains can result in redundant parameter calculations, wasting resources and increasing maintenance costs. Therefore, to verify the effectiveness of the FTS method in the stability analysis of complex GFL/GFM interaction systems, a comprehensive analysis of the attractor domain results is still necessary.

Specifically regarding the first aspect, it considers the impact of different frequency components of M3C on the attraction domain under varying control parameters. Based on Fig. 14(a), whether the parameters increase or decrease, changes in the ML side control parameters have a more significant effect on the system's attraction domain. Further analysis shows that, under typical grid strength ($SCR=1.5$), appropriately increasing the hybrid index R can optimize its sensitivity to novel stability influences. In addition, a detailed comparison of outer control parameters and PLL control parameters on the relatively sluggish MI side is studied. It reveals that the influence of the

MI side's PLL parameters aligns with that of the outer control parameters from ML side, but is more moderate, as shown in Fig. 14(b).

Finally, concerning the second aspect related to grid strength, Fig. 14(b) provides a comprehensive comparison based on different R and SCR. It concludes that although increasing the proportion of the GFM converter can enhance the system's large-signal stability under typical grid conditions ($SCR = 1.5$), this effect diminishes significantly as grid strength increases. It indicates that the GFM converter has weaker resistance to large-signal disturbances under strong grid condition and is more susceptible to instability due to interfrequency interaction characteristics. Consequently, it is essential to specifically optimize the mixed ratio and control parameters based on grid strength and disturbance types, transforming interfrequency interaction characteristics into advantageous forces for enhancing system stability.

In summary, both the GFL/GFM hybrid ratio factor and the interaction factor in the analysis of the system's large-signal stability mechanism demonstrate that, compared to the classical TS fuzzy theory, the FTS method effectively reduces computational complexity to improve efficiency. Moreover, the significant reduction in conservatism makes the attractor domain results more accurate. For nonlinear stability analysis of complex power systems with multiple power electronic devices and control strategy coupling, the FTS method can provide quick and accurate conclusions, which is beneficial for engineering practice in topology design and parameter optimization.

V. Conclusion

In the interconnected system of M3C and GFM/GFL hybrid control strategies converters, various typical large disturbances can lead to different unstable modes due to the interactions of their power electronic devices. To address the challenges of high-order dynamics, strong nonlinearity, and multifrequency coupling in large-signal stability analysis, this article proposes a fuzzy tensor space method. It simplifies the complex of 2^p exponential-level membership function to a constant level of $(p+1)$. By integrating the fuzzy tensor space mapping area with the LMI functional problem, the conservatism is reduced by 42%. Based on the more efficient and accurate analysis results, it is determined that under the same power fluctuation fault conditions, a higher mixed ratio R of GFM converters results in stronger system stability. In addition, incorporating the interfrequency interaction characteristics of M3C reveals that the sensitivity of ML side control parameters to the attraction domain is higher, especially under conditions of a greater R. Furthermore, when considering various SCR, it is studied that this enhancement effect of the GFM converter diminishes under strong grid conditions. These conclusions are significant for the parameter design and stability optimization of hybrid multifrequency power electronic converter interaction systems. The superiority and effectiveness of the proposed method and results are verified through the combination of attraction domains and experimental validation. However, this hybrid configuration involving direct parallel operation of inverters with different control strategies represents only one variant of the GFL/GFM hybrid control strategy. In future work, further research is required on the large-signal stability of other variants, such as direct switching techniques, along with a comparative analysis of their results. Equation (40) shown at the bottom of this page.

Appendix
Specific Example Analysis of Solving Dimensionality Curse

To facilitate a more detailed analysis of the linear independent combinations within the membership function equation space, an example with $p = 3$ will be presented. Based on TS fuzzy theory, there are $2^p = 8$ specific fuzzy rules, as outlined below

1) *Fuzzy Rule 1:* If $g_1(\boldsymbol{x}) = \underline{g}_1, g_2(\boldsymbol{x}) = \underline{g}_2, g_3(\boldsymbol{x}) = \underline{g}_3$, the local system fuzzy matrix $\boldsymbol{A}_1(\underline{g}_1, \underline{g}_2, \underline{g}_3)$ could describe the system as $\dot{\boldsymbol{x}}(t) = f(\boldsymbol{x}) = \boldsymbol{A}_1\boldsymbol{x}$.
2) *Fuzzy Rule 2:* If $g_1(\boldsymbol{x}) = \underline{g}_1, g_2(\boldsymbol{x}) = \bar{g}_2, g_3(\boldsymbol{x}) = \underline{g}_3$, the local system fuzzy matrix $\boldsymbol{A}_2(\underline{g}_1, \bar{g}_2, \underline{g}_3)$ could describe the system as $\dot{\boldsymbol{x}}(t) = f(\boldsymbol{x}) = \boldsymbol{A}_2\boldsymbol{x}$.
3) *Fuzzy Rule 3:* If $g_1(\boldsymbol{x}) = \underline{g}_1, g_2(\boldsymbol{x}) = \underline{g}_2, g_3(\boldsymbol{x}) = \bar{g}_3$, the local system fuzzy matrix $\boldsymbol{A}_3(\underline{g}_1, \underline{g}_2, \bar{g}_3)$ could describe the system as $\dot{\boldsymbol{x}}(t) = f(\boldsymbol{x}) = \boldsymbol{A}_3\boldsymbol{x}$.
4) *Fuzzy Rule 4:* If $g_1(\boldsymbol{x}) = \underline{g}_1, g_2(\boldsymbol{x}) = \bar{g}_2, g_3(\boldsymbol{x}) = \bar{g}_3$, the local system fuzzy matrix $\boldsymbol{A}_4(\underline{g}_1, \bar{g}_2, \bar{g}_3)$ could describe the system as $\dot{\boldsymbol{x}}(t) = f(\boldsymbol{x}) = \boldsymbol{A}_4\boldsymbol{x}$.
5) *Fuzzy Rule 5:* If $g_1(\boldsymbol{x}) = \bar{g}_1, g_2(\boldsymbol{x}) = \underline{g}_2, g_3(\boldsymbol{x}) = \underline{g}_3$, the local system fuzzy matrix $\boldsymbol{A}_5(\bar{g}_1, \underline{g}_2, \underline{g}_3)$ could describe the system as $\dot{\boldsymbol{x}}(t) = f(\boldsymbol{x}) = \boldsymbol{A}_5\boldsymbol{x}$.

$$
\begin{cases}
\dot{x}_1 = \frac{\left(3u_{cq}^{FM0}C_{FM}-2D\right)x_1+3\left(x_4+i_d^{FM0}\right)x_2+3C_{FM}\left(x_1+\omega_{FM}^0\right)\left(x_3+u_{cq}^{FM0}\right)x_2+3u_{cd}^{FM0}C_{FM}\left(x_1+\omega_{FM}^0\right)x_3+3u_{cd}^{FM0}x_4}{2J} \\
\dot{x}_2 = \frac{3u_{cd}^{FM0}u_{cq}^{FM0}C_{FM}x_1+3u_{cq}^{FM0}C_{FM}\left(x_1+\omega_{FM}^0\right)x_2+3\left(x_5+i_q^{FM0}\right)x_3+3C_{FM}\left(x_1+\omega_{FM}^0\right)\left(x_2+u_{cd}^{FM0}\right)x_3+3u_{cq}^{FM0}x_5}{2\Lambda} \\
\dot{x}_{12} = 1.5\left(x_9+i_d^{FL0}\right)\dot{x}_7+1.5\left(x_{10}+i_q^{FL0}\right)\dot{x}_8+1.5\left(x_7+u_{cd}^{FL0}\right)\dot{x}_9+1.5\left(x_8+u_{cq}^{FL0}\right)\dot{x}_{10} \\
\dot{x}_{13} = \frac{\left(3L_L-L_g^{FM}\right)x_2+L_Lx_7-R_g^{FM}\left(2L_L-L_g^{FM}\right)x_{13}+\omega_{FM}^0L_g^{FM}\left(2L_L-L_g^{FM}\right)x_{14}-L_g^{FM}x_{15}-\left(4R_LL_L-R_LL_g^{FM}-R_g^{FM}L_L\right)x_{27}}{\left(2L_L-L_g^{FM}\right)/L_g^{FM}} \\
\dot{x}_{14} = \frac{\left(3L_L-L_g^{FM}\right)x_3+L_Lx_8-\omega_{FM}^0L_g^{FM}\left(2L_L-L_g^{FM}\right)x_{13}-R_g^{FM}\left(2L_L-L_g^{FM}\right)x_{14}-L_g^{FM}x_{16}-\left(4R_LL_L-R_LL_g^{FM}-R_g^{FM}L_L\right)x_{28}}{\left(2L_L-L_g^{FM}\right)/L_g^{FM}} \\
\dot{x}_{19} = -0.5k_p^{MIP}L_g\left(x_{23}+i_d^{MI0}\right)x_{19}+k_i^{MIP}x_{20}-0.5k_p^{MIP}\left(R_g+\omega_{MI}^0L_g\right)x_{22}+E_gk_p^{MIP}x_{23} \\
\dot{x}_{27} = \frac{x_2+x_7-2x_{15}-\left(2R_L-R_g^{FM}\right)x_{27}-\left(-2\omega_{ML}^0L_L+\omega_{FM}^0L_g^{FM}\right)x_{28}}{2L_L-L_g^{FM}} \\
\dot{x}_{28} = \frac{x_3+x_8-2x_{16}-\left(2\omega_{ML}^0L_L-\omega_{FM}^0L_g^{FM}\right)x_{27}-\left(2R_L-R_g^{FM}\right)x_{28}}{2L_L-L_g^{FM}}.
\end{cases}
\tag{40}
$$

. . . . . .

7) *Fuzzy Rule 7:* If $g_1(\boldsymbol{x}) = \bar{g}_1, g_2(\boldsymbol{x}) = \underline{g}_2, g_3(\boldsymbol{x}) = \bar{g}_3$, the local system fuzzy matrix $\boldsymbol{A}_7(\bar{g}_1, \underline{g}_2, \bar{g}_3)$ could describe the system as $\dot{\boldsymbol{x}}(t) = f(\boldsymbol{x}) = \boldsymbol{A}_7\boldsymbol{x}$.
8) *Fuzzy Rule 8:* If $g_1(\boldsymbol{x}) = \bar{g}_1, g_2(\boldsymbol{x}) = \bar{g}_2, g_3(\boldsymbol{x}) = \bar{g}_3$, the local system fuzzy matrix $\boldsymbol{A}_8(\bar{g}_1, \bar{g}_2, \bar{g}_3)$ could describe the system as $\dot{\boldsymbol{x}}(t) = f(\boldsymbol{x}) = \boldsymbol{A}_8\boldsymbol{x}$.

Based on the aforementioned theory, the number of linearly independent sets in this case is $p + 1 = 4$. If each fuzzy rule is denoted by X_i, and without loss of generality, X_1, X_2, X_3 and X_7 is selected as the representative group example Y for analysis. Specifically, by observing X_4, it can be demonstrated that it can be expressed as a linear combination of Y, with the following specific expression:

$$X_4 = X_3 - X_1 + X_2 \Longrightarrow$$
$$A_4\left(\underline{g}_1 = \underline{g}_1 - \underline{g}_1 + \underline{g}_1, \bar{g}_2 = \underline{g}_2 - \underline{g}_2 + \bar{g}_2, \bar{g}_3 = \bar{g}_3 - \underline{g}_3 + \underline{g}_3\right). \tag{41}$$

Similarly, other fuzzy rules, such as $X_8 = X_7 - X_1 + X_2$, can be expressed using Y, and this can be written as

$$X_5 = X_7 - X_3 + X_1, X_6 = X_7 - X_3 + X_2. \tag{42}$$

In summary, the example for $p = 3$ clearly demonstrates the validity of the aforementioned principles. This conclusion can be established through mathematical induction, and the corresponding theoretical proof is presented in greater detail in the main body of the article.

REFERENCES

[1] R. Cuzmar, A. Montenegro, A. Mora, J. Pereda, and R. P. Aguilera, "Constrained MPC for intercluster energy control of modular multilevel matrix converters," *IEEE Trans. Ind. Electron.*, vol. 71, no. 7, pp. 7766–7776, Jul. 2024.

[2] P. Bontemps, D. Biner, C. Münch-Alligné, and D. Dujic, "Online loss calculation and optimization of an M3C-driven externally excited SM," *IEEE Trans. Ind. Electron.*, vol. 71, no. 6, pp. 5608–5617, Jun. 2024.

[3] B. Zhao, X. Wang, X. Wang, and S. Liu, "Upgrading transmission capacity by altering HVAC into fractional frequency transmission system," *IEEE Trans. Power Del.*, vol. 37, no. 5, pp. 3855–3862, Oct. 2022.

[4] Y. Meng et al., "Comparative economic analysis of low frequency AC transmission system for the integration of large offshore wind farms," *Renewable Energy*, vol. 179, pp. 1955–1968, 2021.

[5] Y. Gu and T. C. Green, "Power system stability with a high penetration of inverter-based resources," *Proc. IEEE*, vol. 111, no. 7, pp. 832–853, Jul. 2023.

[6] F. Han, X. Zhang, M. Li, F. Li, and W. Zhao, "Stability control for grid-connected inverters based on hybrid-mode of grid-following and grid-forming," *IEEE Trans. Ind. Electron.*, vol. 71, no. 9, pp. 10750–10760, Sep. 2024.

[7] J. Wang, X. Zhang, and M. Li, "Transient stability analysis and improvement of multiparalleled virtual synchronous generators grid-connected system," *IEEE Trans. Emerg. Sel. Topics Power Electron.*, vol. 12, no. 4, pp. 4094–4105, Aug. 2024.

[8] W. Jiang, M. Wang, X. Li, Z. Xu, X. Zhang, and X. Wu, "Autonomous finite-time backstepping control for decentralized economic power dispatch in DC microgrids toward large-signal stability," *IEEE Trans. Ind. Electron.*, vol. 71, no. 3, pp. 2942–2954, Mar. 2024.

[9] Z. Duan, Y. Meng, Y. Duan, H. Zhang, X. Wang, and X. Wang, "Large-signal stability analysis and enhancement of modular multilevel matrix converter under power fluctuation based on T-S fuzzy model theory," *IEEE Trans. Power Electron.*, vol. 38, no. 11, pp. 14601–14613, Nov. 2023.

[10] X. Fu et al., "Large-signal stability of grid-forming and grid-following controls in voltage source converter: A comparative study," *IEEE Trans. Power Electron.*, vol. 36, no. 7, pp. 7832–7840, Jul. 2021.

[11] H. Zhang, M. Mehrabankhomartash, M. Saeedifard, Y. Zou, Y. Meng, and X. Wang, "Impedance analysis and stabilization of point-to-point HVDC systems based on a hybrid AC–DC impedance model," *IEEE Trans. Ind. Electron.*, vol. 68, no. 4, pp. 3224–3238, Apr. 2021.

[12] J. Lyu, X. Zhang, X. Cai, and M. Molinas, "Harmonic state-space based small-signal impedance modeling of a modular multilevel converter with consideration of internal harmonic dynamics," *IEEE Trans. Power Electron.*, vol. 34, no. 3, pp. 2134–2148, Mar. 2019.

[13] D. Marx, P. Magne, B. Nahid-Mobarakeh, S. Pierfederici, and B. Davat, "Large signal stability analysis tools in DC power systems with constant power loads and variable power loads: A review," *IEEE Trans. Power Electron.*, vol. 27, no. 4, pp. 1773–1787, Apr. 2012.

[14] Y. Li et al., "Synchronization stability of multiple VSGs embedded power system with controller limits," *IEEE Trans. Power Syst.*, vol. 40, no. 1, pp. 834–849, Jan. 2025.

[15] Z. Qiu, C. Duan, W. Yao, P. Zeng, and L. Jiang, "Adaptive Lyapunov function method for power system transient stability analysis," *IEEE Trans. Power Syst.*, vol. 38, no. 4, pp. 3331–3344, Jul. 2023.

[16] H. Zheng, L. Zhou, P. Sun, and W. Lu, "Large-signal stability analysis for VSC-HVDC systems based on mixed potential theory," *IEEE Trans. Power Del.*, vol. 35, no. 4, pp. 1939–1948, Aug. 2020.

[17] Z. Wu et al., "A novel method for estimating the region of attraction for DC microgrids via Brayton-Moser's mixed potential theory," *IEEE Trans. Smart Grid*, vol. 14, no. 4, pp. 3313–3316, Jul. 2023.

[18] T. Huang, S. Gao, and L. Xie, "A neural Lyapunov approach to transient stability assessment of power electronics-interfaced networked microgrids," *IEEE Trans. Smart Grid*, vol. 13, no. 1, pp. 106–118, Jan. 2022.

[19] Y. Liu et al., "An improved neural Lyapunov method for transient stability assessment of networked microgrids," *IEEE Trans. Smart Grid*, vol. 15, no. 2, pp. 1410–1422, Mar. 2024.

[20] Q. Song, J. Chen, K.-H. Loo, J. Chen, and P. Chen, "Large-signal stability analysis of two-stage cascaded DC/DC converter systems using sum-of-squares programming," *IEEE Trans. Power Electron.*, vol. 39, no. 2, pp. 2076–2085, Feb. 2024.

[21] Z. Duan, Y. Meng, T. Wang, H. Zhang, X. Wang, and X. Wang, "Large-signal stability analysis using Takagi-Sugeno fuzzy model theory for fractional frequency transmission system under grid faults," *IEEE Trans. Power Syst.*, vol. 39, no. 1, pp. 2227–2238, Jan. 2024.

[22] Y. Du, Y. Men, L. Ding, and X. Lu, "Large-signal stability analysis for inverter-based dynamic microgrids reconfiguration," *IEEE Trans. Smart Grid*, vol. 14, no. 2, pp. 836–852, Mar. 2023.

[23] S. Liu, X. Li, M. Xia, Q. Qin, and X. Liu, "Takagi-Sugeno multimodeling-based large signal stability analysis of DC microgrid clusters," *IEEE Trans. Power Electron.*, vol. 36, no. 11, pp. 12670–12684, Nov. 2021.

[24] G. Cui, Z. Chu, and F. Teng, "Control-mode as a grid service in software-defined power grids: GFL vs GFM," *IEEE Trans. Power Syst.*, vol. 40, no. 1, pp. 314–326, Jan. 2025.

[25] R. Ma et al., "Dominant transient equations of grid-following and grid-forming converters by controlling-unstable- equilibrium-point-based participation factor analysis," *IEEE Trans. Power Syst.*, vol. 39, no. 3, pp. 4818–4834, May 2024.

[26] T.-T. Nguyen, T. Vu, S. Paudyal, F. Blaabjerg, and T. L. Vu, "Grid-forming inverter-based wind turbine generators: Comprehensive review, comparative analysis, and recommendations," 2022, *arXiv:2203.02105*.

[27] Z. Duan, Y. Meng, T. Wang, B. Zhao, X. Wang, and X. Wang, "Fuzzy Lyapunov function based stability analysis of hybrid multiple-frequency system with low frequency offshore wind power integration," *Int. J. Elect. Power Energy Syst.*, vol. 164, 2025, Art. no. 110437.

[28] Z. Zhao et al., "Fully decoupled branch energy balancing control method for modular multilevel matrix converter based on sequence circulating components," *CSEE J. Power Energy Syst.*, vol. 10, no. 1, pp. 235–247, Jan. 2024.

[29] Z. Yu, Z. Zhang, and Z. Xu, "Electromechanical transient modeling of the low-frequency AC system with modular multilevel matrix converter stations," *IEEE Trans. Power Syst.*, vol. 39, no. 1, pp. 921–933, Jan. 2024.

[30] R. Himker and A. Mertens, "Operating-point-optimized control strategy for modular multilevel converters in low-frequency AC transmission systems," *IEEE Trans. Power Electron.*, vol. 39, no. 2, pp. 2334–2350, Feb. 2024.

[31] S. Liu, X. Wang, L. Ning, B. Wang, M. Lu, and C. Shao, "Integrating offshore wind power via fractional frequency transmission system," *IEEE Trans. Power Del.*, vol. 32, no. 3, pp. 1253–1261, Jun. 2017.

Ziyue Duan (Student Member, IEEE) received the B.S. degree in electrical engineering, in 2019, from Xi'an Jiaotong University, Xi'an, China, where he is currently working toward the Ph.D. degree in electrical engineering.

He became a Visiting Scholar with Imperial College London, London, U.K., in 2024. His research interests include small and large signal stability analysis of power-electronic-based power system.

Yongqing Meng (Member, IEEE) received the master's and Ph.D. degrees in electrical engineering from Xi'an Jiaotong University, Xi'an, China, in 2002 and 2007, respectively.

He is currently an Associate Professor with the School of Electrical Engineering, Xi'an Jiaotong University. His research interests include renewable energy generation, HVDC transmission systems, fractional frequency transmission system, FACTS, and stability analysis and control of power system.

Peiqi Zhao (Student Member, IEEE) received the B.S. degree from the Henan Institute of Science and Technology, Henan, China, in 2017, and the M.S. degree from Xidian University, Xi'an, China in 2020, respectively. She is currently working toward the Ph.D. degree with Xi'an Jiaotong University, Xi'an, all in electrical engineering.

Her research interests include renewable energy generation systems, HVDC, and stability analysis and control of power system.

Shuhao Yan (Student Member, IEEE) was born in Xi'an, Shaanxi, China in 1996. He received the B.S. and M.S. degrees in electrical engineering in 2019 and 2022, respectively, from the Xi'an Jiaotong University, Xi'an, China, where he is currently working toward the Ph.D. degree in electrical engineering.

His research interests include topology and control of modular multilevel converters based on modular multilevel techniques.

Xiuli Wang (Senior Member, IEEE) received the B.S., M.S., and Ph.D. degrees in electrical engineering from Xi'an Jiaotong University, Xi'an China, in 1982, 1985, and 1997, respectively.

She has been with Xi'an Jiaotong University, since 1985, where she is currently a Professor with the School of Electrical Engineering, Her research interests include the power market, reliability assessment of power system, and integration of renewable power.

Xifan Wang (Fellow, IEEE) received the Graduation degree in electrical engineering from Xi'an Jiaotong University, Xi'an, China, in 1957.

From 1983 to 1986, he was a Visiting Scientist with Cornell University, Ithaca, NY, USA. From 1991 to 1994, he worked as a Visiting Professor with the Kyushu Institute of Technology, Kitakyushu, Japan. He is currently a Member of the Chinese Academy of Sciences. His research interests include the analysis, operation, and planning of power systems and novel transmission schemes.